

## Optical and Quantum Communications

### RLE Group

Optical and Quantum Communications Group

### Academic and Research Staff

Professor Jeffrey H. Shapiro, Dr. Franco N. C. Wong, Dr. Marco Fiorentino

### Graduate Students

Marius A. Albota, Baris I. Erkmen, Pavel V. Gorelik, Saikat Guha, Taehyun Kim, Christopher E. Kuklewicz, Onur Kuzucu, Mohsen Razavi, Brent J. Yen

The central theme of our programs has been to advance the understanding of optical and quantum communication, radar, and sensing systems. Broadly speaking, this has entailed: (1) developing system-analytic models for important propagation, detection, and communication scenarios; (2) using these models to derive the fundamental limits on system performance; and (3) identifying, and establishing through experimentation the feasibility of, techniques and devices which can be used to approach these performance limits.

## 1. Quantum Information and Communication

### Sponsors

Air Force Research Laboratory - Cooperative Agreement F30602-01-2-0546

Army Research Office - Grant DAAD-19-00-1-0177

DARPA Contract HR0011-05-C-0063

HP-MIT Alliance

MIT Lincoln Laboratory

NIST - Grant 60NANB5D1004

Office of Naval Research - Contract N00014-03-1-0869

Office of Naval Research - Contract N00014-02-1-0717

### Project Staff

Professor Jeffrey H. Shapiro, Dr. Franco N. C. Wong, Dr. Marco Fiorentino, Marius A. Albota, Saikat Guha, Taehyun Kim, Christopher E. Kuklewicz, Onur Kuzucu, Mohsen Razavi, Brent J. Yen

We are embarked on research in the area of quantum information technology whose goal is to enable the quantum-mechanical information transmission, storage, and processing needed for future applications in quantum computing and quantum communication. Our theoretical work in this area has focused on architectural designs for long-distance teleportation and multi-party entanglement transmission, and on novel applications of entanglement. Of particular interest has been the identification of high-performance means for generating the polarization-entangled photons needed for many quantum information applications, including teleportation, entanglement-based quantum positioning and clock synchronization, and quantum secret sharing. We are also interested in the fundamental limits on classical information transmission that are due to the quantum noise of Bosonic channels. Our main experimental work is focused on generation and application of entanglement sources with high brightness and wavelength tunability. In addition, we are interested in novel entanglement sources and their applications in quantum logic gates, enhanced quantum measurements, and quantum teleportation protocols.

Architectural Analysis The preeminent obstacle to the development of quantum information technology is the difficulty of transmitting quantum information over noisy and lossy quantum communication channels, recovering and refreshing the quantum information that is received, and

then storing it in a reliable quantum memory. We lead a team of researchers from MIT and Northwestern University (NU) that has proposed, analyzed, and is developing the key technological elements of a novel architecture for the singlet-state approach to quantum teleportation [1,2]. A simple block diagram of this architecture is shown in Fig. 1. It consists of an ultrabright narrowband source of polarization-entangled photons pairs ( $P$ ), connected to a pair of trapped Rb atom quantum memories ( $M$ ) by transmission through  $L$ -km-long lengths of standard telecommunication fiber.

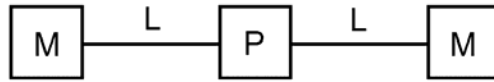


**Figure 1.** Schematic of long-distance quantum communication system:  $P$  = ultrabright narrowband source of polarization-entangled photon pairs;  $L$  =  $L$  km of standard telecommunication fiber;  $M$  = trapped atom quantum memory.

Each  $M$  block in Fig. 1 is a quantum memory in which a single ultracold  $^{87}\text{Rb}$  atom is confined by a  $\text{CO}_2$ -laser trap in an ultra-high vacuum chamber with cryogenic walls within a high-finesse single-ended optical cavity. An abstract representation of the relevant hyperfine levels for such a memory is given in Fig. 2(a). A 795 nm photon in an arbitrary polarization can be absorbed, transferring the qubit from the photon to the degenerate  $B$  levels of Fig. 2(a), and thence to long-lived storage levels, by coherently driving the  $B$ -to- $D$  transitions. By means of optically-off-resonant (OOR) transitions, the Bell states of two atoms in a single vacuum-chamber trap can be converted into superposition states of one of the atoms. All four Bell measurements needed for the Bennett *et al.* singlet-state teleportation process [3] can then be made, sequentially, by detecting the presence (or absence) of fluorescence as an appropriate sequence of OOR laser pulses is applied to the latter atom. The Bell-measurement results (two bits of classical information) in one memory can be sent to a distant memory, where (at most) two additional OOR pulses are needed to complete the state transformation process. More details on this memory, and its use in teleportation, are given in [4].

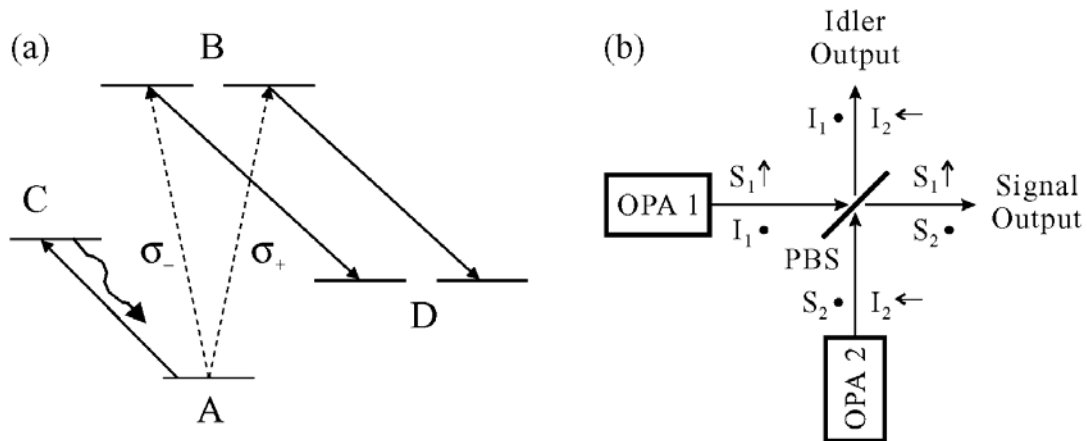


**Figure 2.** Essential components of singlet-state quantum communication system from Fig. 1. Left (a), simplified atomic-level schematic of the trapped Rb atom quantum memory:  $A$ -to- $B$  transition occurs when one photon from an entangled pair is absorbed;  $B$ -to- $D$  transition is coherently driven to enable storage in the long-lived  $D$  levels;  $A$ -to- $C$  cycling transition permits nondestructive determination of when a photon has been absorbed. Right (b), ultrabright narrowband source of polarization-entangled photon pairs: each optical parametric amplifier (OPA1 and OPA2) is type-II phase matched; for each optical beam the propagation direction is  $z$ , and  $x$  and  $y$  polarizations are denoted by arrows and bullets, respectively; PBS, polarizing beam splitter.

The  $P$  block in Fig. 1 is an ultrabright narrowband source of polarization-entangled photon pairs [5], capable of producing  $\sim 10^6$  pairs/sec in  $\sim 30$  MHz bandwidth by appropriately combining the signal and idler output beams from two doubly-resonant type-II phase matched optical parametric amplifiers (OPAs), as sketched in Fig. 2(b). The importance of our resonant approach to entanglement generation is the need to achieve high flux within the narrow linewidth of the Rb atom memory; existing parametric downconverter sources of entanglement are far too broadband to permit useful transmission rates in the Fig. 1 architecture.

During the past year our performance analysis efforts have been concentrated on comparing the merits of the MIT/NU approach to entanglement distribution and teleportation with an alternative architecture — due to Duan, Lukin, Cirac and Zoller (DLCZ) [6] — that relies of atomic ensembles, rather than single trapped atoms. The DLCZ protocol for entangling two widely-separated atomic ensembles is shown schematically in Fig. 3(a). Two ensembles — each consisting of  $N_a$  identical atoms with  $\Lambda$ -level configurations, as shown in Fig. 3(b) — are coherently pumped using a weak, off-resonant laser such that  $p_c$ , the probability of occurrence of a Raman transition from the ground level  $|g\rangle$  to the meta-stable level  $|s\rangle$  is very low. The forward-scattered Stokes light from such a Raman transition in each ensemble is routed over an  $L_0$ -km-long path to the midpoint between the locations of the two ensembles. There, the outputs from these optical channels are combined on a 50/50 beam splitter (BS) prior to measurement by a pair of single-photon detectors (SPDs),  $D_1$  and  $D_2$ , whose dark counts are assumed to be negligible. Suppose that only one ensemble undergoes a Raman transition, as heralded by one and only one of the detectors registering a click. Then, because the ensembles are coherently pumped and the beam splitter erases which-path information, the two ensembles are left in the entangled state

$$|\Psi_k\rangle = (|0\rangle_L|1\rangle_R + (-1)^k|1\rangle_L|0\rangle_R)/2^{1/2}, \quad \text{for } k = 1, 2$$

when  $D_k$  is the detector that registered the click, and  $|0\rangle_A$ ,  $|1\rangle_A$  for  $A = L, R$  and the ensemble ground states and symmetric collective excited state of the left ( $L$ ) and right ( $R$ ) ensembles.

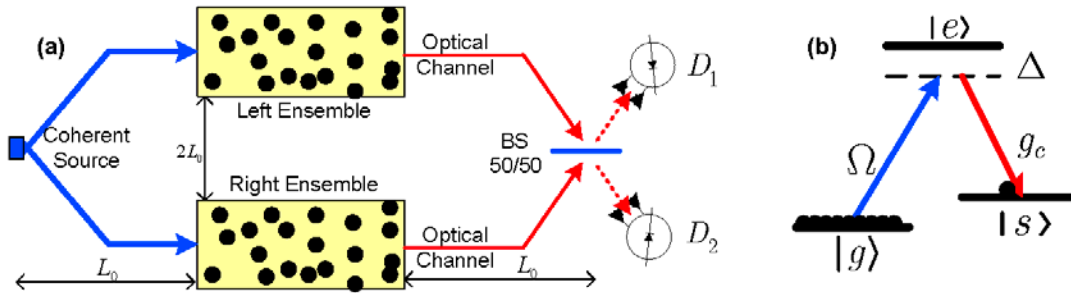


**Figure 3.** (a) DLCZ architecture for entanglement distribution. A coherent laser source, located at the midpoint between two atomic ensembles, stimulates Raman transitions in these ensembles. Occurrence of a single click on one — and only one — detector heralds the protocol's success, i.e., the atomic ensembles are then expected to be entangled. (b)  $\Lambda$ -level structure for the atoms in the ensembles:  $\Omega$  is the Rabi frequency associated with the off-resonant (detuning  $\Delta$ ) pumping of the  $|g\rangle \rightarrow |e\rangle$  transition and  $g_c$  is the coupling coefficient for the  $|e\rangle \rightarrow |s\rangle$  transition.

The DCLZ approach to teleportation builds on the Fig. 3 entanglement distribution scheme and is shown in Fig. 4. The atomic ensembles  $\{L_1, R_1\}$  and  $\{L_2, R_2\}$  are assumed to have been entangled in singlet states by means of the Fig. 3 arrangement, where  $\{L_1, L_2\}$  are co-located as are  $\{R_1, R_2\}$ . The qubit to be teleported is the state

$$|\psi_{in}\rangle_{12} = d_0|1\rangle_1|0\rangle_2 + d_1|0\rangle_1|1\rangle_2, \quad \text{where } |d_0|^2 + |d_1|^2 = 1,$$

that is stored in ensembles  $\{I_1, I_2\}$ , which are co-located with  $\{L_1, L_2\}$ . The objective is to transfer the  $\{d_0, d_1\}$  coherence to the  $\{R_1, R_2\}$  ensembles. This is accomplished, in a conditional fashion, by pumping the  $|s\rangle \rightarrow |e\rangle$  transitions of the  $\{L_1, L_2, I_1, I_2\}$  ensembles with strong retrieval pulses that guarantee the emission of anti-Stokes ( $|e\rangle \rightarrow |g\rangle$  transition) photons from every ensemble that was in its symmetric collective atomic state. These photons are routed to the 50/50 beam splitters and detected by four single-photon detectors. Observation of one and only one click from detectors  $\{D_1^I, D_1^L\}$  and one and only one click from detectors  $\{D_2^I, D_2^L\}$  heralds completion of the DLCZ teleportation protocol. Any other detection event constitutes a teleportation failure. This is why DLCZ teleportation is said to be conditional.

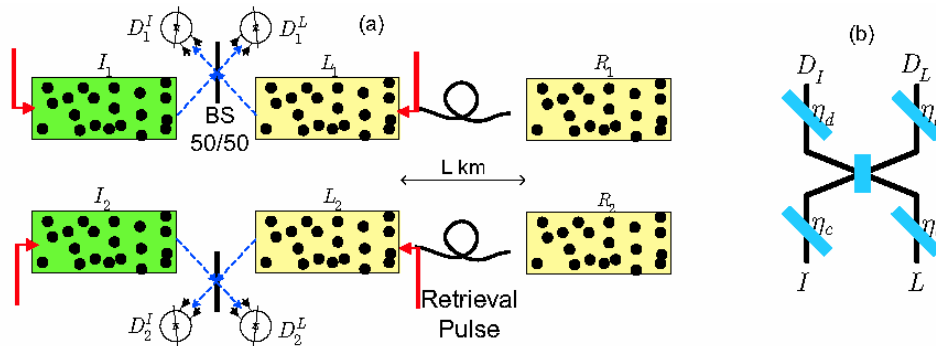
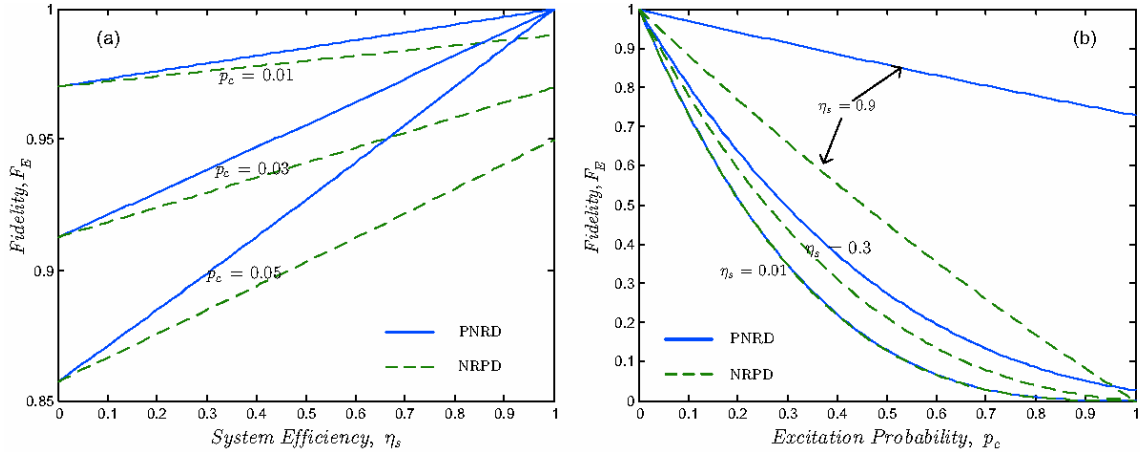


**Figure 4.** (a) DLCZ architecture for conditional teleportation. Two pairs of entangled ensembles  $\{L_1, R_1\}$ ,  $\{L_2, R_2\}$  are used to teleport the quantum state of ensembles  $\{I_1, I_2\}$  to ensembles  $\{R_1, R_2\}$ . Strong retrieval pulses, which are near-resonant with the  $|s\rangle \rightarrow |e\rangle$  transition, are used to pump ensembles  $\{L_1, L_2, I_1, I_2\}$ , recovering anti-Stokes photons from every ensemble that was in its symmetric collective atomic state. Detection of a photon by one, and only one, of the single-photon detectors in each measurement module heralds completion of the protocol. (b) Notional model for the measurement modules in (a): beam splitters with vacuum-state quantum noise injected through their free input ports account for all loss and inefficiency effects; the single-photon detectors are assumed to have unity quantum efficiencies.

Previous analyses of the DLCZ architecture [6,7] are not sufficient to permit quantitative comparison with our entanglement-distribution and teleportation performance analyses for the MIT/NU architecture [8]. We have used the Gaussian entangled-state characterization of the atomic ensembles and their associated Stokes light to evaluate the fidelity and throughput of the DLCZ entanglement-distribution protocol [9]. Our analysis, summarized below, reveals important distinctions between the DLCZ and MIT/NU architectures. It focuses on the error events that result from the occurrence of multiple Raman transitions in the atomic ensembles, and it includes the effects of propagation loss, and sub-unity detector quantum efficiency. Moreover, it considers single-photon detectors that are incapable of distinguishing multiple-photon events from single-photon events, which we term non-resolving photon detectors (NRPDs), and single-photon detectors that do have such a capability, which we term photon-number resolving detectors (PNRDs). As will be seen, our work reveals a hitherto unexpected need for PNRDs in the DLCZ approach to long-distance teleportation.

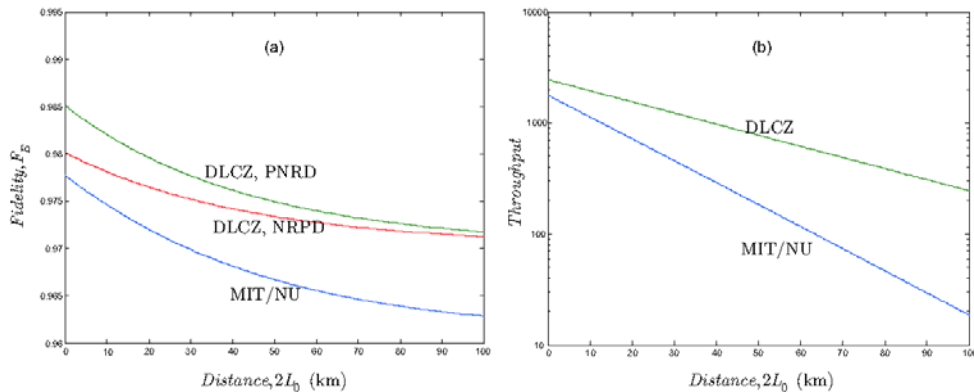
Figure 5 shows the dependence of the DLCZ architecture's entanglement fidelity,  $F_E$ , on its system efficiency  $\eta_s$  and the excitation probability  $p_c$ . Here,  $F_E$  measures the degree to which the atomic ensembles in Fig. 3(a) are left in the desired entangled state, given that a heralding event has occurred, and  $\eta_s$  lumps together all propagation and measurement-module transmission factors, which are assumed to be identical for each ensemble-to-measurement-module path. For  $\eta_s \ll 1$  and  $p_c \ll 1$ , this figure shows that both the PNRD and NRPD systems have the same  $F_E$  behavior, given by  $F_E \approx 1 - 3p_c$ , in accord with the preliminary results reported in the DLCZ paper [6]. We also see that number-resolving detectors can tolerate much higher excitation probabilities than non-resolving detectors, because of their ability to identify and ignore the increasingly-likely occurrence of multiple Raman emissions.

The Fig. 5 results presume perfectly coherent pumping of the two ensembles. This is a rather stringent assumption, in that these two ensembles will be separated by considerable distance. When the laser fields pumping the two ensembles have phases that are independent, identically distributed, zero-mean, variance  $\sigma_\theta^2$ , Gaussian random variables, we have shown that high-fidelity entanglement distribution requires that  $\sigma_\theta^2 \ll 1$  be maintained.



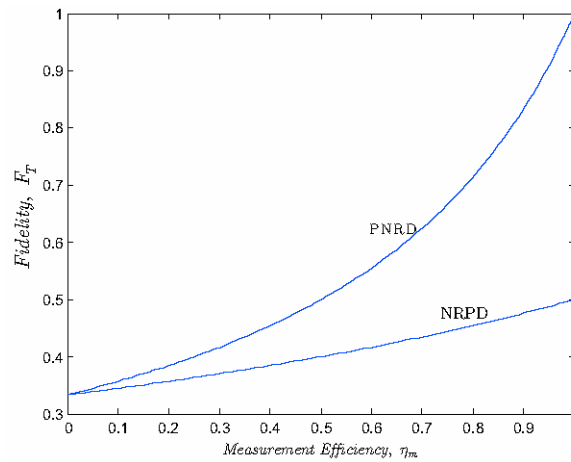
**Figure 5.** Entanglement fidelity,  $F_E$ , versus system efficiency,  $\eta_s$ , for DLCZ entanglement distribution. (b) Entanglement fidelity,  $F_E$ , versus excitation probability,  $p_c$ .

Figure 6 compares the throughput and entanglement fidelity behavior of the DLCZ and MIT/NU architectures as functions of end-to-end path length. Both systems are assumed to have perfect coherent pumping, to operate at a 500 kHz cycling rate, and to employ fibers with 0.2 dB/km propagation loss. The DLCZ excitation probability and the MIT/NU OPA normalized pump powers are both set to 0.001. The detector quantum efficiencies in the DLCZ system are 0.5 and the OPA-to-memory fixed loss in the MIT/NU system is 5 dB. We see from Fig. 6 that both systems achieve high entanglement fidelity under these operating conditions, with the DLCZ architecture having a superior throughput-versus-distance scaling. This scaling advantage is readily explained: the DLCZ architecture only needs one photon to successfully traverse  $L_0$  km in order to achieve entanglement distribution whereas the MIT/NU architecture needs two photons to successfully traverse this distance.



**Figure 6.** Performance comparison of the MIT/NU and DLCZ entanglement-distribution architectures. (a) Entanglement fidelity versus total distance between quantum memories in km. (b) Throughput (entangled pairs/sec) versus total distance between quantum memories in km. The parameter values for these plots are given in the text.

Figure 7 plots the teleportation fidelity, i.e., the degree to which an arbitrary qubit is successfully teleported, achieved by the DLCZ architecture versus the measurement efficiency,  $\eta_m$ , i.e., the product of the efficiency factors shown in each branch of the Fig. 5(b) measurement module. Here we see that high-efficiency operation with a photon-number resolving detector is essential to obtaining high-quality teleportation in the DLCZ architecture. Moreover, such high-quality performance is only obtained on a conditional basis in the DLCZ architecture, as its heralding event will not occur on every trial of the teleportation protocol. In contrast, the MIT/NU architecture yields unconditional, high-fidelity teleportation [8], and has no need for high quantum efficiency PNRDs. Furthermore, although Fig. 6 strongly favors the DLCZ architecture for long-distance entanglement distribution, that figure neglects an important consideration. Both the DLCZ and MIT/NU systems need coherent pumping — of two atomic ensembles for the DLCZ system, and of two OPAs for the MIT/NU system — and Fig. 6 presumes that perfect pump coherence has been realized for both. However, the difficulty of approaching perfect coherent pumping differs dramatically for these two architectures. The MIT/NU architecture needs to coherently pump two co-located OPAs. This capability has already been demonstrated in our initial bidirectional downconverter experiments [10]. The DLCZ architecture requires coherent pumping of two widely-separated atomic ensembles. This is a very challenging task that has yet to be demonstrated.



**Figure 7.** Fidelity of DLCZ teleportation,  $F_T$ , versus measurement efficiency  $\eta_m$ .

**High-Flux Polarization Entanglement Source** In recent years most entanglement sources have been based on spontaneous parametric downconversion (SPDC) in a noncollinearly propagating, angle phase-matched crystal, such as beta barium borate (BBO) [11]. We have taken a different approach to entanglement generation that is based on periodically-poled potassium titanyl phosphate (PPKTP) with collinear propagation of the pump, signal, and idler fields. In a single-beam configuration we have previously obtained very good results: 99% quantum-interference visibility with a coincidence flux of 300/s/mW of pump power. We have also measured the Clauser, Horne, Shimony, and Holt (CHSH) form of Bell's inequality violation [12], obtaining a value of  $2.711 \pm 0.017$  [13]. However, in both noncollinear and collinear configurations, spatial filtering (aperture), spectral filtering (interference filter), and temporal filtering (timing compensation crystal) are necessary for generating polarization entanglement at the expense of significantly reduced flux. Recently we have demonstrated a bidirectionally pumped SPDC geometry for generating polarization-entangled photons at high flux without the need for spatial, spectral, or temporal filtering [10]. We have achieved a ten-fold increase in coincidence flux with a yield of 12,000/s/mW of pump power in a 3-nm bandwidth centered at 797 nm. The phase of the polarization-entangled output state is controlled by a servo on the pump interferometer [10].

More recently we have tested an improved version of the bidirectionally pumped SPDC by incorporating the PPKTP crystal inside a Sagnac interferometer, as shown in Fig. 8. A 10-mm-long PPKTP crystal with a 10.0- $\mu\text{m}$  grating period is pumped by a fiber-coupled ultraviolet (UV) laser at 405 nm for generating polarization entanglement at 810 nm. The pump enters the Sagnac interferometer through a dual-wavelength polarizing beam splitter (PBS), which separates the pump light into its horizontal ( $H$ ) and vertical ( $V$ ) polarization components. The relative amplitude and phase between the pump's  $H$  and  $V$  components are set by the half-wave plate (HWP) and quarter-wave plate (QWP) placed before the interferometer. This pump control eliminates the need for pump phase stabilization in the original bidirectional pumping setup [10].

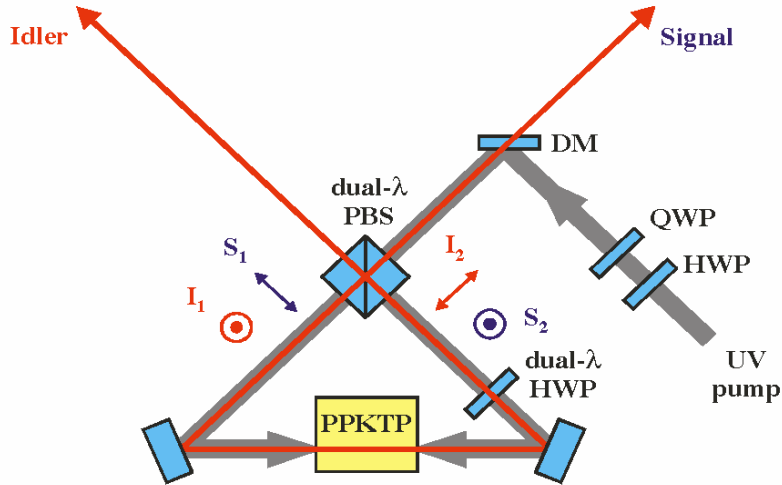


**Figure 8.** Schematic of bidirectionally-pumped SPDC in a Sagnac interferometer configuration. The dual-wavelength PBS combines the two downconverted outputs to form polarization-entangled signal and idler beams that may have different wavelengths. The relative amplitude and phase of the pump's  $H$ - and  $V$ -polarized components are set by the HWP and QWP. HWP, half-wave plate; QWP, quarter-wave plate; PBS, polarizing beam splitter.

The PPKTP crystal is set up for frequency-degenerate type-II phase matching with orthogonally polarized signal and idler outputs. The dual-wavelength HWP rotates the  $V$ -polarized pump component to be  $H$ -polarized, along the crystal's  $x$  axis, which is required for SPDC in PPKTP. Bidirectional pumping thus effectively creates two identical coherently-pumped downconverters. We rotate the outputs of one of the beams by  $90^\circ$  with the dual-wavelength HWP, and combine the two downconverted beams at the dual-wavelength PBS, whose outputs are polarization entangled independent of the output frequencies and propagation directions. We have effectively engineered a decoherence-free subspace in which all output photon pairs are polarization entangled. There is complete indistinguishability (spatially, spectrally, and temporally) at the output. This makes it impossible to tell from which downconverter an output photon originates. Hence the output from the Fig. 8 setup is a coherent superposition of the two downconverted beams [5]. A picture of the compact setup is shown in Fig. 9. The state of the polarization-entangled output is given by

$$|\psi\rangle = (|H\rangle_1|V\rangle_2 - e^{i\phi}|V\rangle_1|H\rangle_2) / \sqrt{2},$$

where the phase  $\phi$  is equal to the pump phase set by the pump's HWP and QWP, plus a fixed offset phase that is related to material dispersion of the interferometer. As a result, the state of the output can be precisely controlled by simply changing the relative phase between the  $H$ - and  $V$ -polarized components of the pump input.

Figure 10 shows preliminary results of two-photon coincidence measurements for the Sagnac SPDC source output as a function of idler polarization analysis angle for a given signal polarization analysis angle of either  $0^\circ$  or  $45^\circ$ . We have obtained high visibilities of over 97% for both signal angles. Within a 1-nm bandwidth filter centered at 810 nm we have obtained a flux of 5,800/s/mW of pump power, which is 45% higher than our first generation bidirectionally pumped SPDC [10]. This compact and phase-stable Sagnac source may prove to be useful for many quantum optical applications, such as quantum key distribution and linear optics quantum computing. We also intend to use the Sagnac source for the generation of hyperentangled photons that are entangled in both momentum and polarization degrees of freedom.

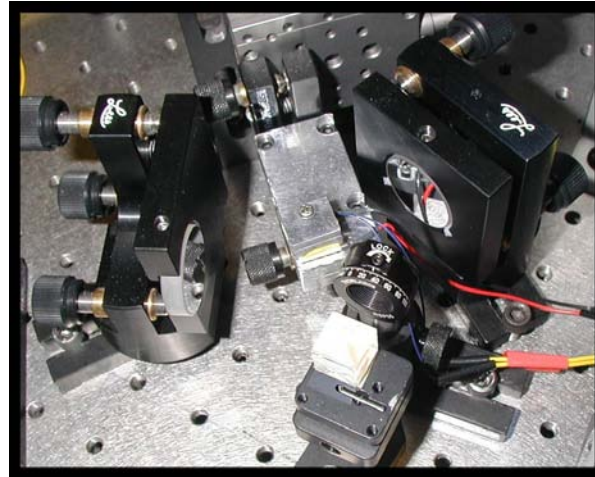


**Figure 9.** Bidirectionally pumped Sagnac SPDC source, showing the two flat mirrors, the crystal holder and oven, and the dual-wavelength half-wave plate and dual-wavelength polarizing beam splitter.

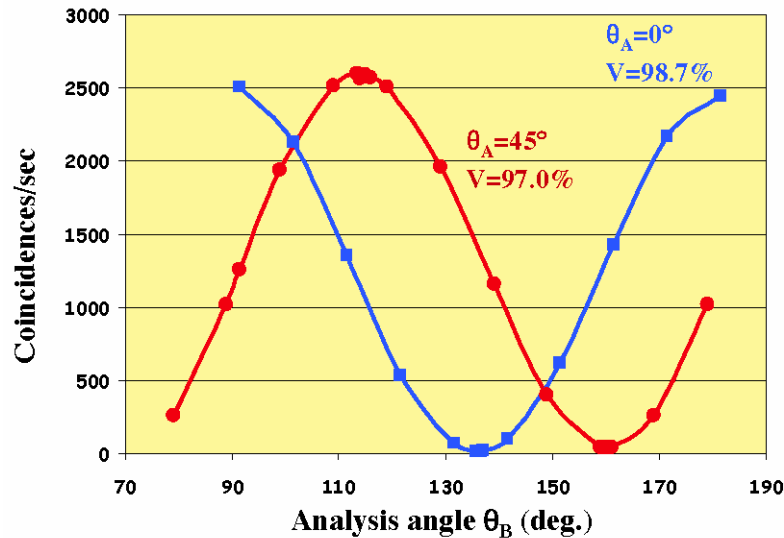


**Figure 10.** Plot of two-photon coincidence counts as a function of idler polarization analysis angle  $\theta_B$  for signal angle  $\theta_A$  set at either  $0^\circ$  (blue squares) or  $45^\circ$  (red circles). High visibilities of over 97% indicate high-quality polarization entanglement from the bidirectionally pumped Sagnac SPDC source.

Single-Photon Two-Qubit (SPTQ) Quantum Logic Typical SPDC sources generate photon pairs that are entangled only in their polarization degree of freedom. However, one can view the photons as simply carriers of quantum information and that two or more qubits can be carried by

a single photon. We have recently shown that the polarization and momentum (spatial) degrees of freedom of single photons can be utilized to carry out deterministic quantum logic operations, which we term single-photon two-qubit (SPTQ) quantum logic. SPTQ logic is potentially useful for implementing a few-qubit quantum information processor [14]. A controlled-NOT gate has been demonstrated in which the polarization qubit of a single photon serves as the control qubit while the momentum qubit of the same photon is the target qubit [15]. In a polarization-controlled-NOT (P-CNOT) operation the target qubit flips its bit value if the polarization control qubit is  $|1\rangle$ , but it remains the same if the control qubit is  $|0\rangle$ . We identify the  $H$  and  $V$  polarizations as  $|0\rangle$  and  $|1\rangle$ , and, similarly, right ( $R$ ) and left ( $L$ ), and top ( $T$ ) and bottom ( $B$ ) spatial pathways, as  $|0\rangle$  and  $|1\rangle$ , respectively.

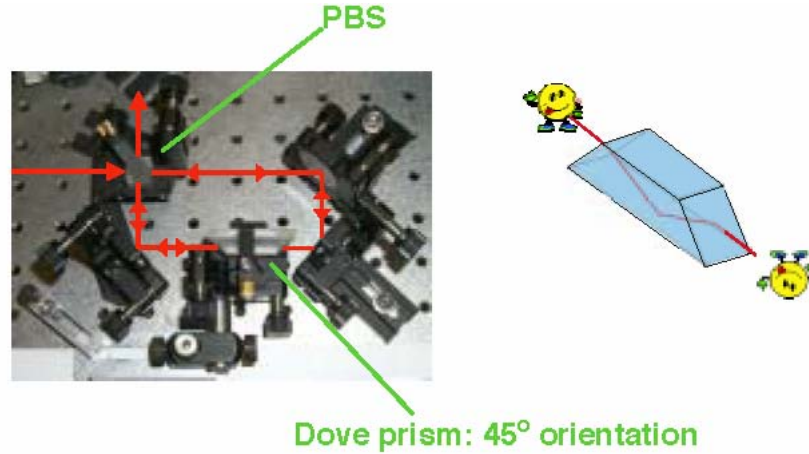


**Figure 11.** P-CNOT gate implementation: a polarization Sagnac interferometer with an embedded dove prism oriented at  $45^\circ$ . A cartoon of the dove prism shows that the image is flipped upside down, but not side to side.

Figure 11 shows the apparatus that realizes the P-CNOT gate. A polarization Sagnac interferometer is formed with an input/output PBS and a dove prism oriented at  $45^\circ$  relative to  $H$  polarization. The PBS separates the input light into its  $H$  and  $V$  polarized components, which travel clockwise and counter-clockwise, respectively. The two polarization components see different dove prism orientations that are orthogonal to each other, resulting in an image orientation that is  $+90^\circ$  and  $-90^\circ$  with respect to the input image. That is, an input beam at the top position emerges at the right (left) side if the polarization is  $H$  ( $V$ ), which corresponds precisely to what a P-CNOT gate does. The experimentally-obtained truth table for the Fig. 11 P-CNOT gate is shown in Fig. 12. It indicates high fidelity gate operation. However, the truth table in Fig. 12 does not say anything about the quantum coherence of the process. This can be indirectly demonstrated by utilizing the P-CNOT gate as an entangler. The P-CNOT gate transforms the product-state input

$$|\Psi_{in}\rangle = \frac{|H\rangle + |V\rangle}{\sqrt{2}} \otimes |R\rangle,$$

into the entangled-state output

$$|\Psi_{out}\rangle = \frac{|HR\rangle + |VL\rangle}{\sqrt{2}},$$

which is a triplet state. This entangled nature of this output state can be demonstrated by projecting the output along the  $(R,L)$  and  $(R \pm L)$  bases and measuring the resulting polarization behavior. We have used this technique to confirm the entangling property of the deterministic P-CNOT gate [15].

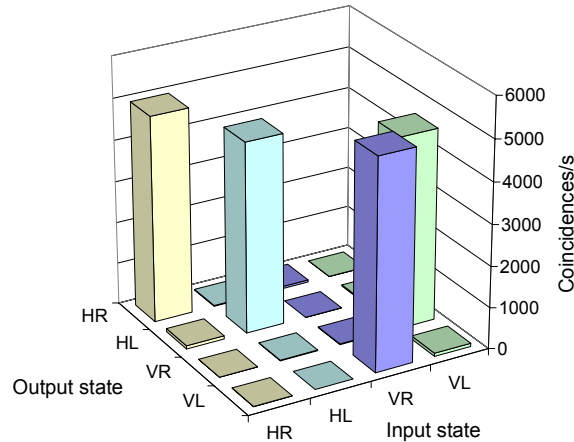


**Figure 12.** Truth table of the P-CNOT gate.

The other type of CNOT gate, the M-CNOT gate, can be simply implemented by use of a HWP in the left (logical “1”) pathway. It is well known that a SWAP gate can be constructed using an M-CNOT gate, a P-CNOT gate, and another M-CNOT gate. We have implemented a SWAP gate and applied it to a pair of momentum-entangled photons [16]. The SWAP operation exchanges the qubit values between the polarization and momentum qubits of single photons. The SWAP would transform a pair of momentum-entangled photons into polarization-entangled photons that are no longer momentum entangled. Figure 13 shows the resulting two-photon coincidence counting measurements in two different polarization angle settings for the signal photons. High visibility confirms the SWAP operation and its gate fidelity. We have also measured the CHSH form of Bell’s inequality violation showing a value of  $2.653 \pm 0.004$  [16]. Together with single-qubit rotations, the CNOT gates form a universal gate set that allows one to perform any unitary transformation for these polarization and momentum qubits. SPTQ quantum logic is robust and efficient and may play an important role in few-qubit quantum information science.

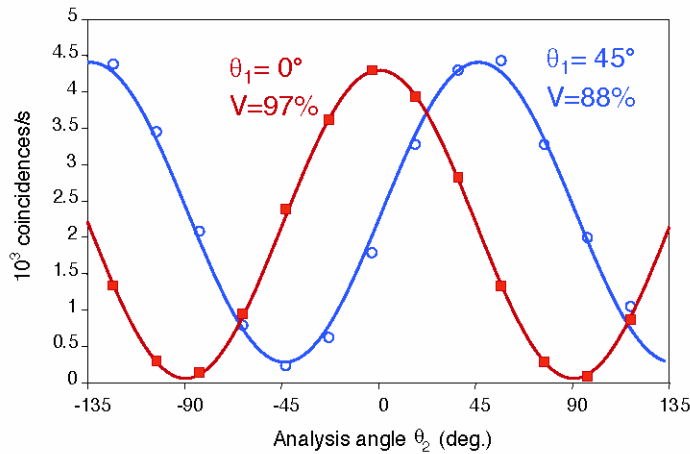


**Figure 13.** Two-photon coincidence measurements as a function of idler analysis angle for verification of polarization entanglement after a SWAP-gate transformation of a pair of momentum-entangled photons.

Coincident-frequency entanglement via extended phase matching Entangled photons are typically generated by SPDC under conventional phase matching condition,  $\Delta k = k_P(\omega_P) - k_S(\omega_P/2) - k_I(\omega_P/2) = 0$ , where  $k$  is the wave vector along the propagation direction for pump ( $P$ ), signal ( $S$ ), and idler ( $I$ ). For cw pumping the signal and idler photons have identical spectra leading to high

visibility for Hong-Ou-Mandel (HOM) interferometric measurements. However, in pulsed pumping the phase matching condition is not met over the entire broad pump spectrum such that the signal and idler output spectra can differ significantly. In other words, pulsed pumping causes the signal and idler photons to be spectrally distinguishable which reduces the HOM visibility. We have theoretically shown that this can be rectified by use of an extended phase matching (EPM) condition [17], in which the first frequency derivative of the phase mismatch is also zero,  $\Delta k'(\omega) = 0$ . Under EPM broadband phase matching for second-harmonic generation has been demonstrated in PPKTP [18], yielding a bandwidth of nearly 70 nm, which is  $\sim 100$ -fold wider than typical second-harmonic generation bandwidths.

We have recently applied the EPM condition to SPDC for generating entangled signal and idler photons that have the same spectral properties under broadband pumping [19]. A femtosecond Ti:S laser with a 6-nm bandwidth at  $\sim 790$  nm was used to generate entangled photons in a PPKTP crystal. The orthogonally-polarized signal and idler outputs were analyzed using a fiber HOM interferometer, composed of a fiber polarizing beam splitter to separate the outputs, a fiber polarization controller to match the two polarizations at the fiber 50-50 beam combiner, and an air gap in the idler path to provide path-length tuning for the HOM measurements. Figure 14 shows the HOM measurements we obtained under cw and pulsed pumping. The high-visibility triangular dips seen in both cases indicate substantial spectral indistinguishability between the signal and idler photons. Our results represent the first high-visibility HOM measurement from pulsed SPDC without the use of an interference filter to restrict the output bandwidth. Moreover, we have measured the pulse widths of individual signal and idler photons in our pulsed-SPDC experiment to be  $\sim 350$ - $380$  fs, as compared to its biphoton coherence time of 1.3 ps. The long biphoton coherence time shows that the two photons are frequency correlated beyond what classical physics allows, i.e., they are coincident-frequency entangled [19]. This novel quantum state may prove useful in a variety of applications such as improved timing measurements beyond the shot-noise limit [20] and linear optics quantum computing.

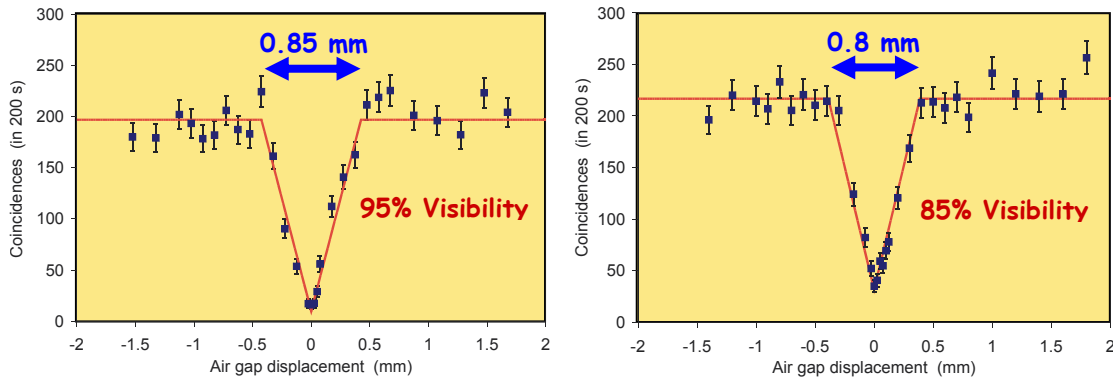


**Figure 14.** Hong-Ou-Mandel interferometric measurements for (left) cw pumping, and (right) pulsed pumping with a 6 nm bandwidth. Inferred biphoton coherence bandwidths are 2.9 nm and 3.2 nm for cw and pulsed pumping, respectively, compared with the theoretically estimated bandwidth of 2.8 nm.

Polarization-Insensitive Frequency Upconversion at 1550 nm The MIT/NU long-distance teleportation protocol depends on one's ability to efficiently translate the quantum state of a photon at  $\sim 1600$  nm to 795 nm for loading the trapped-Rb quantum memory. We have demonstrated a first step toward single-photon quantum state translation by efficiently upconverting cw light at 1550 nm to 631 nm at the single photon level. Based on efficient three-wave mixing in a 4-cm-long periodically-poled lithium niobate (PPLN) crystal, a photon at 1554 nm is mixed with an intense 1064-nm-wavelength pump field, allowing it to be upconverted to 631 nm with 90% conversion efficiency [21]. This upconversion process is polarization sensitive. Only light that is polarized along the PPLN's extraordinary crystal axis is upconverted; the other polarization remains unaffected. It is desirable to achieve efficient upconversion that is not

sensitive to the polarization state, which would allow an arbitrary polarization qubit to be upconverted with polarization-state preservation.

Polarization-insensitive upconversion can be achieved in a bidirectional upconversion scheme in which one polarization component is upconverted in one direction and the orthogonal polarization component in the opposite direction. A schematic is shown in Fig. 15. Consider an input with both  $H$  and  $V$  polarization components, depicted as red arrows and dots in Fig. 15. The fixed-polarization upconverter transfers only  $V$ -polarized light to a shorter wavelength, depicted in green. A dual-wavelength Faraday mirror rotates both the unconverted  $H$ -polarized light and the upconverted  $V$ -polarized light by  $90^\circ$ . On their return trip through the upconverter crystal, the  $H$ -polarized upconverted (green) light is not phase matched and therefore it is transmitted unchanged. The  $V$ -polarized unconverted (red) light is upconverted in the second pass through the upconverter. By rotating the output polarization, the input polarization state is restored in the output state at a new wavelength.

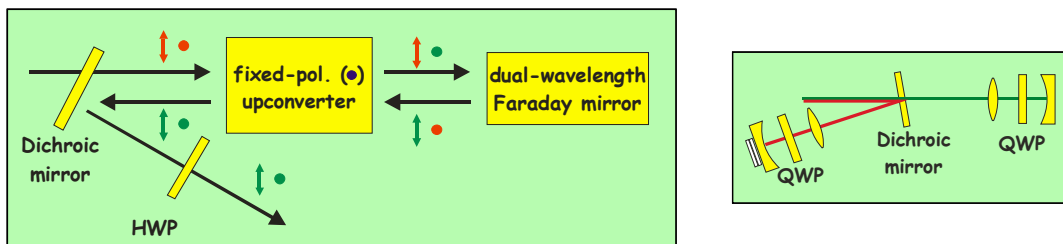


**Figure 15.** Schematic of polarization-insensitive upconversion. The dual-wavelength Faraday mirror is a Michelson interferometer, shown in the right panel. HWP, half-wave plate; QWP, quarter-wave plate.

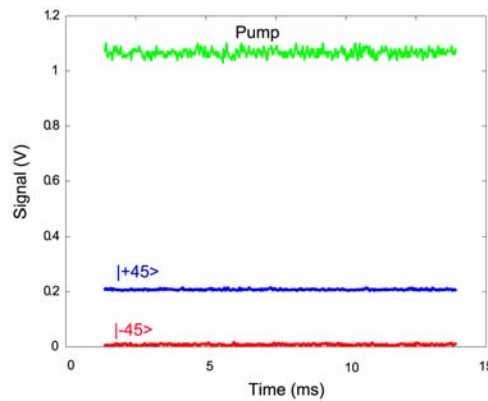


**Figure 16.** Output traces for the upconverted light analyzed along  $+45^\circ$  and  $-45^\circ$  polarization for an input  $+45^\circ$  polarized light. The monitored circulating pump power is also displayed.

In our implementation a standing-wave cavity with an embedded nonlinear crystal allows upconversion to occur in both directions for a fixed polarization. A standing-wave cavity for the 1064-nm pump produces a circulating power of  $\sim 15$  W from an input of  $\sim 400$  mW. The dual-wavelength Faraday mirror implementation is shown in Fig. 15, right panel, using a Michelson interferometer and a QWP-mirror combination for each wavelength. It is important that the relative phase between the unconverted and upconverted light be stabilized in order to maintain the polarization state of the input light. Moreover, the overall upconversion efficiency for both directions should be the same. Figure 16 shows the output light analyzed at  $\pm 45^\circ$  for input light that is polarized at  $45^\circ$  with the Michelson interferometer being path stabilized. For a circulating pump power of 15 W, we have reached an intrinsic upconversion efficiency of only 50%. In the

future, a higher pump input power or a higher finesse cavity can be used to boost the efficiency to near unity. Polarization-insensitive upconversion is not only essential for quantum information processing, but it is also a valuable tool for efficient wavelength translation in many classical applications such as optical communication through the air, water, or in fiber.

Classical Capacity of Free-Space Optical Communication A principal goal of quantum information theory is evaluating the information capacities of important communication channels. At present — despite the many efforts that have been devoted to this endeavor [22] — exact capacity results are known for only a handful of channels. Recently, we have begun addressing this capacity problem for a broad class of Bosonic channels, viz., those involving loss and thermal noise. The basic construct starts from the Holevo-Schumacher-Westmoreland theorem [23,24], which states that the classical capacity of a quantum channel characterized by a trace-preserving, completely-positive (TPCP) map  $E$  is given by

$$C = \sup_n (C_n / n)$$

where

$$C_n = \max_{p_j, \sigma_j} \chi(p_j, E^{\otimes n}[\sigma_j])$$

is the capacity achieved in  $n$  channel uses,  $\{p_j\}$ ,  $\{\sigma_j\}$  are, respectively, the sets of prior probabilities and input density operators for the information symbols  $\{j\}$ , and

$$\chi(p_j, \sigma_j) = S\left(\sum_j p_j \sigma_j\right) - \sum_j p_j S(\sigma_j)$$

defines the Holevo information  $\chi$  in terms of the von Neumann entropy  $S$ . The supremum in this capacity development is necessitated by the fact that Holevo information may be superadditive.

Our primary interest lies in Bosonic channels [25-28], specifically those associated with free-space propagation [26-28], but we have also addressed waveguide propagation [25]. Prior to our efforts, the major extant capacity result was for lossless — and hence noiseless — propagation [29,30]. We have derived narrowband and wideband capacity results for the pure-loss Bosonic channel, in which the propagation loss — channel transmissivity  $\eta < 1$  — is accompanied by the minimal amount of quantum noise (vacuum-state quantum noise) that is required by quantum mechanics [26]. It turns out that the Holevo information is not superadditive for this channel, and random coding over coherent states achieves capacity.

For far-field, single-spatial-mode, line-of-sight propagation over an  $L$ -m-long path between circular apertures of areas  $A_t$  and  $A_r$ , we have obtained the capacity curves shown in Fig. 17 for optimum reception, heterodyne detection, and homodyne detection [26,27]. As suggested by the figure, heterodyne detection is asymptotically optimum at high average power levels.

In addition to the pure-loss channel, in which only vacuum-state quantum noise is injected, we have made substantial progress toward establishing capacity results for two other important channels. The first is the thermal-noise channel, in which loss is accompanied by injection of quantum noise from an isotropic mixture of coherent states. The second is the classical-noise channel, in which classical isotropic Gaussian noise is added to an otherwise lossless channel. The latter models a lossy channel with post-propagation optical amplification used to offset the loss. We have developed reasonably tight lower and upper bounds on the capacity of these channels [27,28]. These bounds are consistent with the conjecture that capacity is achieved — for the thermal-noise and classical-noise channels — by coherent-state encoding as in the pure-loss case. That conjecture would be proven if we could show that coherent-state inputs minimize

the output von Neumann entropy for these channels. Minimum output entropy is an important problem in its own right, and we have made significant headway toward a proof of this property [31,32].

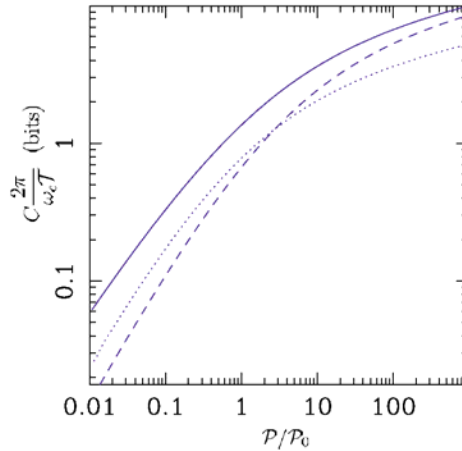


**Figure 17.** Capacities of the far-field free-space optical channel as a function of the input power  $P$  [in this plot,  $P_0 = 2\pi\hbar c^2 L^2 / A_t A_r$ ]. The solid curve is the capacity  $C$ ; the other two curves are the information rates achievable with coherent states and heterodyne detection (dashed curve) or coherent states and homodyne detection (dotted curve). Note that the heterodyne detection performance approaches capacity in the high-power limit.

Our recent efforts have extended the preceding results in several ways. In one line of research, we have considered the multiple-spatial-mode, wideband, free-space propagation channel with soft-aperture (Gaussian-attenuation function) transmitter exit and receiver entrance pupils [33,34]. Although we had previously treated the hard-aperture version of this problem, the soft-aperture formulation admits to closed-form results for the modal transmissivities that underlie channel capacity. More importantly, the Laguerre-Gaussian (LG) modes are eigenfunctions of the soft-aperture propagation geometry. The LG modes have been the subject of considerable interest, within the quantum information community, owing to their carrying orbital angular momentum. Our soft-aperture capacity analysis therefore explores whether these modes enjoy any special merit with respect to classical information transmission. We have shown that the Laguerre-Gaussian mode decomposition for the soft-aperture, free-space channel is related by a unitary transformation to the Hermite-Gaussian (HG) mode decomposition for that channel. These mode sets share a common set of modal transmissivities, hence their channel capacities are identical. Figure 18(a)-(c) plot the capacity achieving power spectra for optimum reception, homodyne detection, and heterodyne detection. In these figures the index  $q$  is a modal degeneracy parameter: maximum transmissivity is achieved by a single (LG or HG) spatial mode (labeled by  $q = 1$ ), there are two (LG or HG) spatial modes with the next highest transmissivity (labeled by  $q = 2$ ), etc. Figure 18(d) shows the capacity behaviors of heterodyne detection, homodyne detection, and optimum reception systems as functions of transmitter power. We see that homodyne detection outperforms heterodyne detection in this multiple-spatial-mode, wideband scenario, but optimum reception enjoys an increasing advantage over homodyne detection as transmitter power is increased.

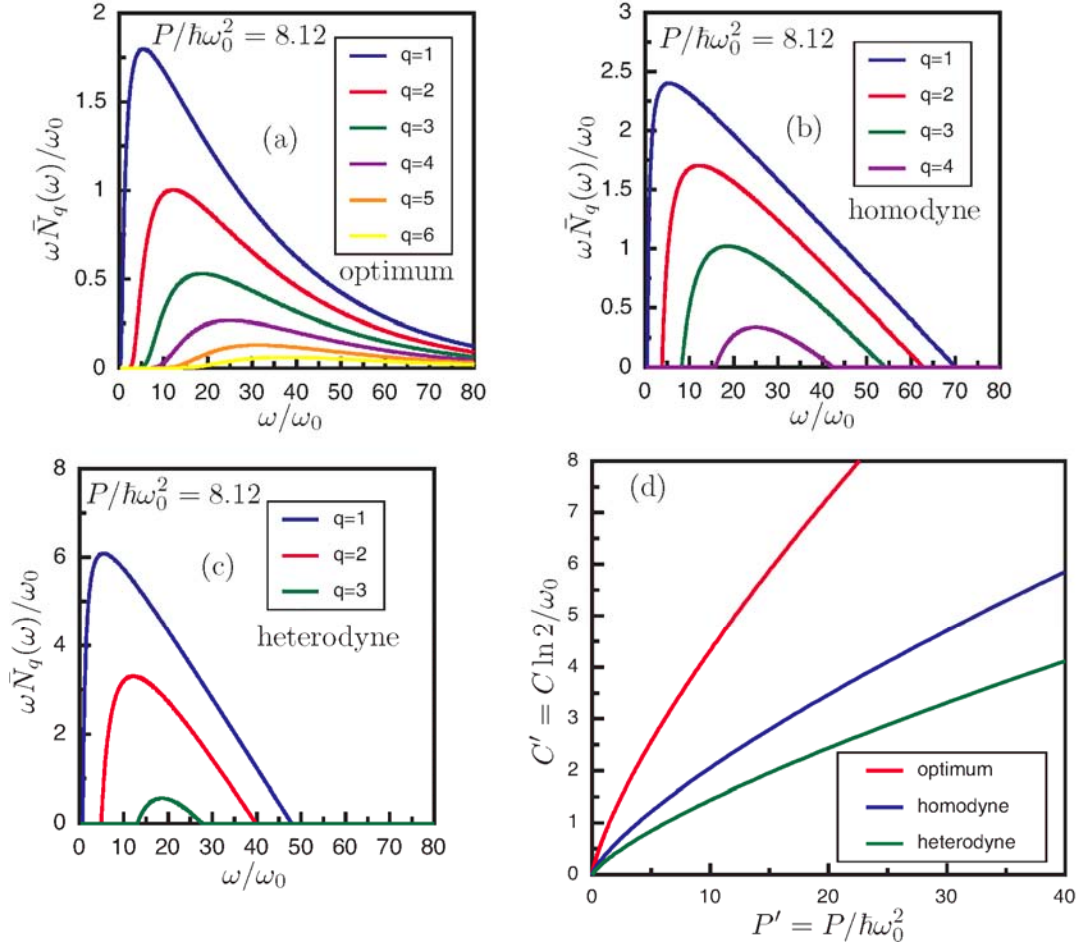


**Figure 18.** Capacity-achieving power spectra (total power =  $P$ ) for wideband, multiple-spatial-mode communication over the scalar, pure-loss, free-space channel: (a) optimum reception uses all spatial modes although spectra are only shown (from top to bottom) for  $1 \leq q \leq 6$ ; (b) homodyne detection uses 10 spatial modes with (from top to bottom)  $1 \leq q \leq 4$ ; (c) heterodyne detection uses 6 spatial modes with (from top to bottom)  $1 \leq q \leq 3$ . (d) Wideband, multiple-spatial-mode capacities for the scalar, pure-loss, free-space channel that are realized with optimum reception (top curve), homodyne detection (middle curve), and heterodyne detection (bottom curve). The capacities, in bits/sec, are normalized by  $\omega_0$ , the frequency at which the product of the transmitter and receiver Fresnel numbers equals unity.

A second area of capacity research has extended our treatment of Bosonic channels to lossy channels with anisotropic (colored) Gaussian noise [33,35]. Assuming that our conjecture for the capacity of the thermal-noise channel is correct, we have been able to establish capacity results for the single-mode channel with anisotropic Gaussian noise by developing a quantum version of the familiar noise-whitening construct of classical communication theory, see Fig. 19. When the anisotropic noise originates from a squeezed state, capacity is achieved with a nonclassical (squeezed-state) input ensemble and exceeds the capacity of the pure-loss channel with the same transmissivity. The squeezed channel noise actually helps the information transmission by affording better communication in the low-noise quadrature than can be realized in the presence of the pure-loss channel's isotropic vacuum-state noise.

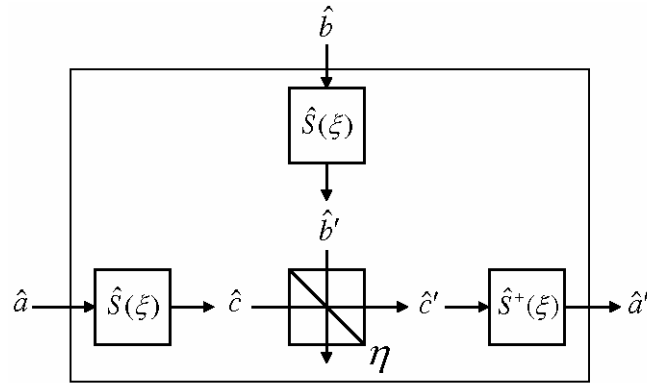


**Figure 19.** Whitening-filter approach to determining the channel capacity of the lossy single-mode channel with anisotropic-Gaussian noise. The inner ( $c$ -to- $c'$ ) channel in this figure shows beam-splitter combining of the transmitter mode,  $c$ , and the noise mode,  $b$ , to produce the channel output,  $c'$ . The noise mode is assumed to be in a zero-mean anisotropic-Gaussian state. The quantum whitening filter is the inverse of the squeeze operator,  $S(\xi)$ , that creates the  $b$ -mode's state from an isotropic-Gaussian state. As a result, the outer ( $a$ -to- $a'$ ) channel in this figure is a thermal-noise channel, whose capacity is assumed known from our prior work.

The third area in which we have been expanding our understanding of classical information transmission over Bosonic channels is the case of multiple-access communications [35-37]. In a multiple-access channel (MAC), two or more senders try to communicate simultaneously to the same receiver. Until our work, almost nothing was known about the classical information-carrying capacity region of a Bosonic MAC. For simplicity, we will limit this summary to our work on the single-mode per sender case, although we have also studied the wideband MAC. Key results from our efforts are shown in Fig. 20. Here, for the two-sender case, we have plotted inner and outer bounds on the achievable rate region, i.e., the range of rates  $(R_1, R_2)$ , in nats per channel use, at which senders 1 and 2 can simultaneously realize error-free communication to their common receiver when both have their average photon numbers constrained. Coherent-state encoding used in conjunction with heterodyne detection has an achievable rate region inside the innermost (dotted-dashed) contour. Coherent-state encoding with optimum (joint measurement over entire code words) reception has an achievable rate region inside the dashed contour, and the ultimate capacity region lies inside the solid contour. We see that the sum-rate  $(R_1 + R_2)$  coherent-state encoding with optimum reception coincides with the sum-rate outer bound, but does not reach the individual  $(R_1$  or  $R_2)$  upper bounds. Because we do not yet know if our individual rate upper bounds are tight, it is interesting to note that we have found a Gaussian (squeezed-state) encoding that reaches deeper into the individual-rate "corners" of Fig. 20 than does coherent-state encoding. This individual-rate improvement, over coherent-state encoding, derives from what we saw for the lossy channel with anisotropic-Gaussian noise. Indeed, the individual-rate improvements shown in Fig. 20 for Gaussian-state encoding originate as follows. To increase the upper limit on  $R_1$  with  $R_2 = 0$ , sender 2 devotes its entire average photon number to sending a zero-mean squeezed state. As a result, sender 1 sees a lossy, anisotropic-Gaussian noise channel, for which we know: (i) that coherent-state encoding is not capacity achieving; and (ii) there is a Gaussian-state encoding for sender 1 that yields an achievable rate larger than that user could realize were there no sender 2, i.e., were sender 1 to be signaling over a pure-loss channel.

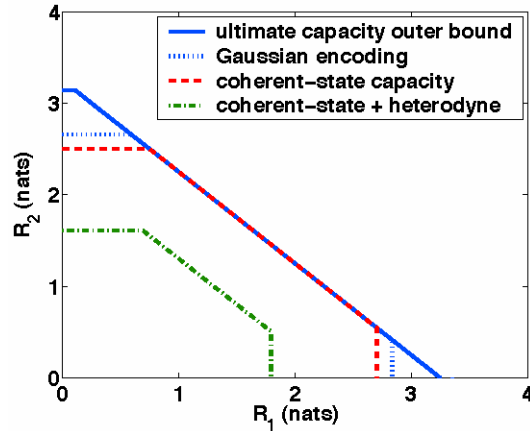


**Figure 20.** Ultimate capacity region of the two-sender, single-mode optical MAC. Inner bounds from coherent-state encoding and Gaussian-state encodings, and outer bounds are shown. This figure assumes each sender has 50% coupling to the common receiver, with the first sender constrained to use no more than 10 photons on average and the second sender constrained to at most 5 photons on average.

## 2. Nonlinear Optics and Precision Measurements

### Sponsor

Office of Naval Research - Contract N00014-02-1-0717

### Project Staff

Professor Jeffrey H. Shapiro, Dr. Franco N. C. Wong, Pavel V. Gorelik

In an era that is increasingly technology driven, precision measurements play a key role in many areas of science and commerce, such as the very successful global positioning system. The recent introduction of femtosecond frequency-comb technology bridges the two extremes of time scales: ultrafast optics in the femtosecond regime and optical frequency metrology at the Hertz and sub-Hertz levels. One significant consequence is the functionality and simplicity afforded by femtosecond technology for use in precision measurements, such as the determination of absolute optical frequencies. We are working in collaboration with Professors Erich Ippen and Franz Kärtner to investigate enabling femtosecond-comb technologies with nonlinear optical techniques.

The main focus of our program is to apply nonlinear optical techniques to improve both the signal-to-noise ratio and stability of self-frequency referencing techniques and to facilitate new applications of femtosecond-comb technology for enhanced functionality. During the last year, we have demonstrated ultra-broadband second-harmonic generation [18] and utilized difference-frequency mixing to enable microwave clockwork without carrier-envelope phase stabilization [38].

In the past year, we have discovered a new nonlinear effect in our work on optical parametric oscillators (OPOs). Typically, when pumped above its threshold, an OPO generates subharmonic signal and idler beams, much like a laser. We have been working on a PPLN OPO that contains two grating sections. The primary OPO section is tuned for 3-to-1 frequency division with input at 532 nm and outputs at  $\sim 798$  nm and  $\sim 1596$  nm. The second section is for second-harmonic generation of  $\sim 798$  nm from the 1596-nm OPO output. This second section has a fan-out grating structure that allows tunability without affecting the first OPO section. We have found that when this second section is detuned, we observe the signature of a secondary OPO driven by the 798 nm output of the primary OPO, as shown in Fig. 21. The signal, which

serves as the pump for the secondary OPO, is clamped over a span of the cavity-length scan. At the same time, no clamping occurs for the idler or the pump. Pump clamping is a standard signature for an OPO because any pump light above the threshold is converted to the signal and idler, leaving the pump clamped at the threshold value.

We have also stabilized the OPO cavity and we were able to observe three outputs near 1600 nm. One of them is the primary idler at  $\sim 1596$  nm. The other two outputs are the signal and idler of the secondary OPO, which can range from  $\pm 30$  nm to  $\pm 120$  nm from the primary idler wavelength, depending on the location of the PPLN's second section that is being pumped. The threshold for the primary OPO is  $\sim 50$  mW, and that of the secondary OPO is  $\sim 180$  mW. Further characterization is underway. This secondary OPO may provide an interesting way to generate tunable outputs.

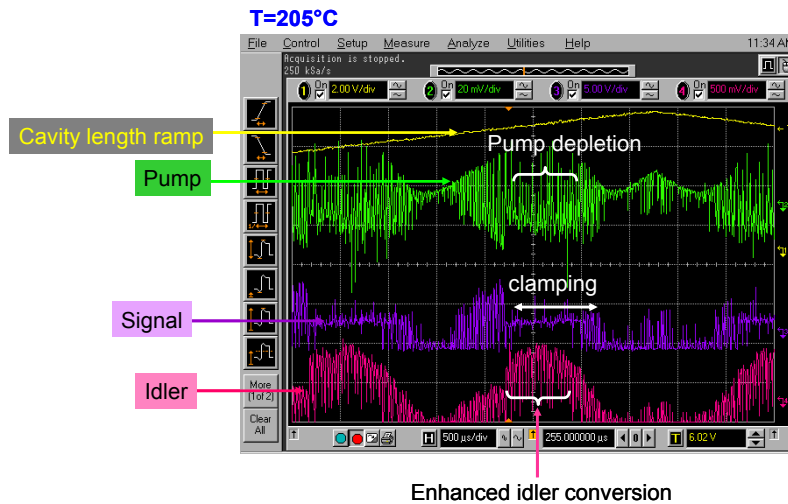


**Figure 21.** Traces of pump (green), signal (purple), idler (pink) as a function of cavity-length scan (yellow). The span over which the signal power is flat indicates that the signal, which serves as the pump for the secondary OPO, is clamped.

## References

1. J. H. Shapiro, "Architectures for Long-Distance Quantum Communication," *New J. Phys.* 4, 47.1-47.18 (2002).
2. S. Lloyd, J. H. Shapiro, F. N. C. Wong, P. Kumar, S. M. Shahriar, and H. P. Yuen, "Infrastructure for the Quantum Internet," *ACM SIGCOMM Comp. Commun. Rev.* 34, 9-20 (2004).
3. C. H. Bennett, G. Brassard, C. Crépeau, R. Jozsa, A. Peres, and W. K. Wootters, "Teleporting and Unknown Quantum State via Dual Classical and Einstein-Podolsky-Rosen Channels," *Phys. Rev. Lett.* 70, 1895-1899 (1993).
4. S. Lloyd, M. S. Shahriar, J. H. Shapiro, and P. R. Hemmer, "Long-Distance Unconditional Teleportation of Atomic States via Complete Bell State Measurements," *Phys. Rev. Lett.* 87, 167903 (2001).
5. J. H. Shapiro and N. C. Wong, "An Ultrabright Narrowband Source of Polarization-Entangled Photon Pairs," *J. Opt. B: Quantum Semiclass. Opt.* 2, L1-L4 (2000).

6. L. M. Duan, M. D. Lukin, J. I. Cirac, and P. Zoller, "Long-Distance Quantum Communication with Atomic Ensembles and Linear Optics," *Nature* (London) 414, 413-418 (2001).
7. L. M. Duan, J. I. Cirac, and P. Zoller, "Three-Dimensional Theory for Interaction between Atomic Ensembles and Free-Space Light," *Phys. Rev. A* 66, 023818 (2002).
8. B. J. Yen and J. H. Shapiro, "Error Models for Long-Distance Qubit Teleportation," *IEEE J. Sel. Topics in Quantum Electron.* 9, 1483-1494 (2003).
9. M. Razavi and J. H. Shapiro, "Long-Distance Quantum Communication with Neutral Atoms," *Proc. SPIE* 5842, 132-143 (2005).
10. M. Fiorentino, G. Messin, C. E. Kuklewicz, F. N. C. Wong, and J. H. Shapiro, "Generation of Ultrabright Tunable Polarization Entanglement without Spatial, Spectral or Temporal Constraints," *Phys. Rev. A* 69, 041801(R) (2004).
11. P. G. Kwiat, E. Waks, A. G. White, I. Appelbaum, and P. H. Eberhard, "Ultrabright Source of Polarization-Entangled Photons," *Phys. Rev. A* 60, R773-R776 (1999).
12. J. F. Clauser, M. A. Horne, A. Shimony, and R. A. Holt, "Proposed Experiment to Test Local Hidden-Variable Theories," *Phys. Rev. Lett.* 23, 880-884 (1969).
13. C. E. Kuklewicz, M. Fiorentino, G. Messin, F. N. C. Wong, and J. H. Shapiro, "High-Flux Source of Polarization-Entangled Photons from a Periodically Poled  $\text{KTiOPO}_4$  Parametric Down-Converter," *Phys. Rev. A* 69, 013807 (2004).
14. K.-Y. Chen, T. Hogg, and R. Beausoleil, "A Quantum Treatment of Public Goods Economics," *Quantum Inf. Process.* 1, 449-469 (2003).
15. M. Fiorentino and F. N. C. Wong, "Deterministic Controlled-NOT Gate for Single-Photon Two-Qubit Quantum Logic," *Phys. Rev. Lett.* 93, 070502 (2004).
16. M. Fiorentino, T. Kim, and F. N. C. Wong, "Single-Photon Two-Qubit SWAP Gate for Entanglement Manipulation," *Phys. Rev. A* 72, 012318 (2005).
17. V. Giovannetti, L. Maccone, J. H. Shapiro, and F. N. C. Wong, "Generating Entangled Two-Photon States with Coincident Frequencies," *Phys. Rev. Lett.* 88, 183602 (2002).
18. F. König and F. N. C. Wong, "Extended Phase Matching of Second-Harmonic Generation in Periodically Poled  $\text{KTiOPO}_4$  with Zero Group-Velocity Mismatch," *Appl. Phys. Lett.* 84, 1644-1646 (2004).
19. O. Kuzucu, M. Fiorentino, M. A. Albota, F. N. C. Wong, and F. X. Kärtner, "Two-Photon Coincident-Frequency Entanglement via Extended Phase Matching," *Phys. Rev. Lett.* 94, 083601 (2005).
20. V. Giovannetti, S. Lloyd, and L. Maccone, "Quantum-Enhanced Positioning and Clock Synchronization," *Nature* (London) 412, 417-419 (2001).
21. M. A. Albota and F. N. C. Wong, "Efficient Single-Photon Counting at  $1.55 \mu\text{m}$  by means of Frequency Upconversion," *Opt. Lett.* 29, 1449-1451 (2004).
22. C. H. Bennett and P. W. Shor, "Quantum Information Theory," *IEEE Trans. Information Theory* 44, 2724-2742 (1998), and references therein.

23. A. S. Holevo, "The Capacity of the Quantum Channel with General Signal States," *IEEE Trans. Information Theory* 44, 269-273 (1998).
24. B. Schumacher and M. D. Westmoreland, "Sending Classical Information via Noisy Quantum Channels," *Phys. Rev. A* 56, 131-138 (1997).
25. V. Giovannetti, S. Lloyd, L. Maccone, and J. H. Shapiro, "Information Rate of a Waveguide," *Phys. Rev. A* 69, 052310 (2004).
26. V. Giovannetti, S. Guha, S. Lloyd, L. Maccone, J. H. Shapiro, and H. P. Yuen, "Classical Capacity of the Lossy Bosonic Channel: the Exact Solution," *Phys. Rev. Lett.* 92, 027902 (2004).
27. V. Giovannetti, S. Guha, S. Lloyd, L. Maccone, J. H. Shapiro, B. J. Yen, and H. P. Yuen, "Classical Capacity of Free-Space Optical Communication," *Quant. Inform. and Comput.* 4, 489-499 (2004).
28. J. H. Shapiro, V. Giovannetti, S. Guha, S. Lloyd, L. Maccone, and B. J. Yen, "Capacity of Bosonic Communications," in *Proceedings of the Seventh International Conference on Quantum Communication, Measurement and Computing*, eds. S. M. Barnett, E. Anderson, J. Jeffers, P. Öhberg, and O. Hirota (American Institute of Physics, 2004).
29. H. P. Yuen and M. Ozawa, "Ultimate Information Carrying Limit of Quantum Systems," *Phys. Rev. Lett.* 70, 363-366 (1993).
30. C. M. Caves and P. D. Drummond, "Quantum Limits on Bosonic Communication Rates," *Rev. Mod. Phys.* 66, 481-537 (1994).
31. V. Giovannetti, S. Guha, S. Lloyd, L. Maccone, and J. H. Shapiro, "Minimum Output Entropy of Bosonic Channels: a Conjecture," *Phys. Rev. A* 70, 032315 (2004).
32. V. Giovannetti, S. Lloyd, L. Maccone, J. H. Shapiro, and B. J. Yen, "Minimum Rényi and Wehrl Entropies at the Output of Bosonic Channels," *Phys. Rev. A* 70, 022328 (2004).
33. J. H. Shapiro, B. J. Yen, S. Guha, and B. I. Erkmen, "Classical Communication in the Presence of Quantum Gaussian Noise," *Proc. SPIE* 5842, 63-73 (2005).
34. J. H. Shapiro, S. Guha, and B. I. Erkmen, "Ultimate Channel Capacity of Free-Space Optical Communications," *J. Opt. Networking*, forthcoming.
35. B. J. Yen, *Multiple-User Quantum Optical Communication* Ph.D. diss., Department of Electrical Engineering and Computer Science, MIT 2004; also Res. Lab. Electron. Technical Rep. 707.
36. B. J. Yen and J. H. Shapiro, "Multiple-Access Bosonic Communications," *Proc SPIE* 5842, 93-104 (2005).
37. B. J. Yen and J. H. Shapiro, "Multiple-Access Bosonic Communications," submitted to *Phys. Rev. A*; e-print quant-ph/0506171.
38. O. D. Mücke, O. Kuzucu, F. N. C. Wong, E. P. Ippen, F. X. Kärtner, S. M. Foreman, D. J. Jones, L.-S. Ma, J. L. Hall, and J. Ye, "Experimental Implementation of Optical Clockwork without Carrier-Envelope Phase Control," *Opt. Lett.* 29, 2806-2808 (2004).

## Publications

### Journal Articles, Published

V. Giovannetti, S. Lloyd, L. Maccone, and J. H. Shapiro, "Information Rate of a Waveguide," *Phys. Rev. A* 69, 052310 (2004).

V. Giovannetti, S. Guha, S. Lloyd, L. Maccone, J. H. Shapiro, B. J. Yen, and H. P. Yuen, "Classical Capacity of Free-Space Optical Communication," *Quant. Inform. and Comput.* 4, 489-499 (2004).

V. Giovannetti, S. Lloyd, L. Maccone, J. H. Shapiro, and B. J. Yen, "Minimum Rényi and Wehrl Entropies at the Output of Bosonic Channels," *Phys. Rev. A* 70, 022328 (2004).

V. Giovannetti, S. Guha, S. Lloyd, L. Maccone, and J. H. Shapiro, "Minimum Output Entropy of Bosonic Channels: a Conjecture," *Phys. Rev. A* 70, 032315 (2004).

M. A. Albota and F. N. C. Wong, "Efficient Single-Photon Counting at 1.55  $\mu\text{m}$  by means of Frequency Upconversion," *Opt. Lett.* 29, 1449-1451 (2004).

J.-J. Zondy, D. Kolker, and F. N. C. Wong, "Dynamical Signatures of Self Phase-Locking in a Triply Resonant Optical Parametric Oscillator," *Phys. Rev. Lett.* 93, 043902 (2004).

M. Fiorentino and F. N. C. Wong, "Deterministic Controlled-NOT Gate for Single-Photon Two-Qubit Quantum Logic," *Phys. Rev. Lett.* 93, 070502 (2004).

V. Giovannetti, S. Lloyd, L. Maccone, J. H. Shapiro, and F. N. C. Wong, "Conveyor-Belt Clock Synchronization," *Phys. Rev. A* 70, 043808 (2004).

P. Kumar, P. Kwiat, A. Migdall, S. W. Nam, J. Vuckovic, and F. N. C. Wong, "Photonic Technologies for Quantum Information Processing," *Quantum Inf. Process.* 3, 215-231 (2004).

S. Lloyd, J. H. Shapiro, F. N. C. Wong, P. Kumar, S. M. Shahriar, and H. P. Yuen, "Infrastructure for the Quantum Internet," *ACM SIGCOMM Comp. Commun. Rev.* 34, 9-20 (2004).

O. D. Mücke, O. Kuzucu, F. N. C. Wong, E. P. Ippen, F. X. Kärtner, S. M. Foreman, D. J. Jones, L.-S. Ma, J. L. Hall, and J. Ye, "Experimental Implementation of Optical Clockwork without Carrier-Envelope Phase Control," *Opt. Lett.* 29, 2806-2808 (2004).

V. Giovannetti, L. Maccone, S. Guha, S. Lloyd, J. H. Shapiro, and B. J. Yen, "Minimum Output Entropy of a Gaussian Bosonic Channel," *International J. Quantum Inform.* 3 153-158 (2005).

M. Razavi and J. H. Shapiro, "Wireless Optical Communications via Diversity Reception and Optical Preamplification," *IEEE Trans. Wireless Commun.* 4, 975-983 (2005).

M. Fiorentino, C. E. Kuklewicz, and F. N. C. Wong, "Source of Polarization Entanglement in a Single Periodically Poled KTiOPO<sub>4</sub> Crystal with Overlapping Emission Cones," *Opt. Express* 13, 127-135 (2005).

O. Kuzucu, M. Fiorentino, M. A. Albota, F. N. C. Wong, and F. X. Kärtner, "Two-Photon Coincident-Frequency Entanglement via Extended Phase Matching," *Phys. Rev. Lett.* 94, 083601 (2005).

S. M. Foreman, A. Marian, J. Ye, E. A. Petrukhin, M. A. Gubin, O. D. Mücke, F. N. C. Wong, E. P. Ippen, and F. X. Kärtner, "Demonstration of a HeNe/CH<sub>4</sub>-based Optical Molecular Clock," *Opt. Lett.* 30, 570-572 (2005).

## Chapter 22. Optical and Quantum Communications

F. König, E. J. Mason, F. N. C. Wong, and M. A. Albota, "Efficient and Spectrally Bright Source of Polarization-Entangled Photons," *Phys. Rev. A* 71, 033805 (2005).

M. Fiorentino, T. Kim, and F. N. C. Wong, "Single-Photon Two-Qubit SWAP Gate for Entanglement Manipulation," *Phys. Rev. A* 72, 012318 (2005).

### Journal Articles, Accepted for Publication

J. H. Shapiro, S. Guha, and B. I. Erkmen, "Ultimate Channel Capacity of Free-Space Optical Communications," *J. Opt. Networking*, forthcoming.

### Journal Articles, Submitted for Publication

B. J. Yen and J. H. Shapiro, "Multiple-Access Bosonic Communications," submitted to *Phys. Rev. A*; e-print quant-ph/0506171.

### Book/Chapters in Books

J. H. Shapiro, V. Giovannetti, S. Guha, L. Maccone, and H. P. Yuen, "Classical Capacity of Free-Space Optical Communication," in *Quantum Information, Statistics, Probability*, ed. O. Hirota (Rinton Press, 2004).

### Meeting Papers, Presented

V. Giovannetti, S. Guha, L. Maccone, J. H. Shapiro, B. J. Yen, and H. P. Yuen, "Information Capacity of Bosonic Channels," paper presented at the 2004 IEEE International Symposium on Inform. Theory, Chicago, Illinois, June 27-July 2, 2004.

J. H. Shapiro, "Quantum Theory of Coincidence Counting: Gaussian States and Quantum Interference," paper presented at the Annual Meeting of the Optical Society of America, Rochester, New York, October 10-14, 2004.

O. D. Mücke, O. Kuzucu, F. N. C. Wong, E. P. Ippen, F. X. Kärtner, S. M. Foreman, D. J. Jones, L.-S. Ma, J. L. Hall, and J. Ye, "Optical Clockwork without Carrier-Envelope Phase Control," paper presented at the 17th IEEE Lasers & Electro-Optics Society Annual Meeting, Rio Mar, Puerto Rico, November 7-11, 2004.

F. X. Kärtner, O. D. Mücke, L. Matos, F. N. C. Wong, D. Kleppner, E. P. Ippen, , S. M. Foreman, A. Marian, J. Ye, E. A. Petrukhin, and M. A. Gubin, "Solid-State Laser Technology for Optical Clocks," paper presented at the International Conference on Lasers, Applications, and Technologies, St. Petersburg, Russia, May 11-15, 2005.

### Meeting Papers, Published

J. H. Shapiro, V. Giovannetti, S. Guha, S. Lloyd, L. Maccone, and B. J. Yen, "Capacity of Bosonic Communications," in *Proceedings of the Seventh International Conference on Quantum Communication, Measurement and Computing*, eds. S. M. Barnett, E. Anderson, J. Jeffers, P. Öhberg, and O. Hirota (American Institute of Physics, 2004).

B. J. Yen and J. H. Shapiro, "Two Problems in Multiple Access Quantum Communication," in *Proceedings of the Seventh International Conference on Quantum Communication, Measurement*

*and Computing*, eds. S. M. Barnett, E. Anderson, J. Jeffers, P. Öhberg, and O. Hirota (American Institute of Physics, 2004).

V. Giovannetti, S. Guha, S. Lloyd, L. Maccone, J. H. Shapiro, and B. J. Yen, "Minimum Bosonic Channel Output Entropies," in *Proceedings of the Seventh International Conference on Quantum Communication, Measurement and Computing*, eds. S. M. Barnett, E. Anderson, J. Jeffers, P. Öhberg, and O. Hirota (American Institute of Physics, 2004).

M. Fiorentino, T. Kim, and F. N. C. Wong, "Single-Photon Two-Qubit Logic Gates," in *Proceedings of the Seventh International Conference on Quantum Communication, Measurement and Computing*, eds. S. M. Barnett, E. Anderson, J. Jeffers, P. Öhberg, and O. Hirota (American Institute of Physics, 2004).

J. H. Shapiro, C. E. Kuklewicz, and F. N. C. Wong, "Quantum Signatures from Singly-Resonant and Doubly-Resonant Parametric Amplifiers," *Digest of Nonlinear Optics: Materials, Fundamentals and Applications*, Waikoloa, Hawaii, August 2-6, 2004.

M. A. Albota, F. N. C. Wong, and J. H. Shapiro, "Polarization-Independent Upconversion for High-Efficiency Photon Counting and Quantum Optical Communication," *Digest of Nonlinear Optics: Materials, Fundamentals and Applications*, Waikoloa, Hawaii, August 2-6, 2004.

B. I. Erkmen and J. H. Shapiro, "Performance Analysis for Near-Field Atmospheric Optical Communications," *Digest of IEEE Global Telecommunications Conference*, Dallas, Texas, November 29 – December 3, 2004.

J. H. Shapiro, B. J. Yen, S. Guha, and B. I. Erkmen, "Classical Communication in the Presence of Quantum Gaussian Noise," *Proc. SPIE 5842*, 63-73 (2005).

B. J. Yen and J. H. Shapiro, "Multiple-Access Bosonic Communications," *Proc SPIE 5842*, 93-104 (2005).

M. Razavi and J. H. Shapiro, "Long-Distance Quantum Communication with Neutral Atoms," *Proc. SPIE 5842*, 132-143 (2005).

O. Kuzucu, M. Fiorentino, M. A. Albota, F. N. C. Wong, and F. X. Kärtner, "Generation of Coincident-Frequency Entangled Photons via Extended Phase Matching," *Proc. 9th International Conference on Squeezed States and Uncertainty Relations*, Besançon, France, May 2-6, 2005.

O. Kuzucu, M. Fiorentino, M. A. Albota, F. N. C. Wong, and F. X. Kärtner, "Coincident-Frequency Entanglement via Extended Phase Matching," *Digest of Quantum Electronics and Laser Science Conference*, Baltimore, Maryland, May 22-27, 2005.

M. A. Albota, F. N. C. Wong, and J. H. Shapiro, "Polarization-Preserving Frequency Conversion for High-Efficiency Photon Counting and Quantum Communication," *Digest of Quantum Electronics and Laser Science Conference*, Baltimore, Maryland, May 22-27, 2005.

J.-J. Zondy, D. Kolker, P. V. Gorelik, and F. N. C. Wong, "Slow Dynamics and Multi-Pair Phase-Locked Oscillation in the Divide-by-3 OPO," *Digest of Conference on Lasers and Electro-Optics and European Quantum Electronics and Laser Science Conference*, Munich, Germany, June 12-17, 2005.

### Theses

B. J. Yen, *Multiple-User Quantum Optical Communication* Ph.D. diss., Department of Electrical Engineering and Computer Science, MIT 2004; also Res. Lab. Electron. Technical Rep. 707.